JGR Atmospheres

RESEARCH ARTICLE
10.1029/2025JD044467

Influence of Variations in Gravity Wave Properties on Cirrus Ice Number Concentrations Produced by Homogeneous Freezing in the Tropical Tropopause Layer

E. J. Jensen[1,2], **M. Corcos**[3], **and B. Kärcher**[4]

[1]NOAA Chemical Sciences Laboratory, Boulder, CO, USA, [2]Cooperative Institute for Research in Environmental Sciences, Boulder, CO, USA, [3]NorthWest Research Associates, Boulder Office, Boulder, CO, USA, [4]Institute for Atmospheric Physics, DLR Oberpfaffenhofen, Weßling, Germany

Key Points:

- High frequency waves dominate the observed vertical wind speed variance and the nucleation of high ice number concentrations in tropical tropopause layer (TTL) cirrus
- Both the wind speed variance and the detailed vertical wind power spectra are important for the nucleated concentration of ice crystals
- Variability in gravity wave properties is an important source of variations in TTL cirrus ice number concentration

Correspondence to:
E. J. Jensen,
ericjj50@gmail.com

Citation:
Jensen, E. J., Corcos, M., & Kärcher, B. (2026). Influence of variations in gravity wave properties on cirrus ice number concentrations produced by homogeneous freezing in the tropical tropopause layer. *Journal of Geophysical Research: Atmospheres*, *131*, e2025JD044467. https://doi.org/10.1029/2025JD044467

Received 29 MAY 2025
Accepted 15 FEB 2026

Abstract In this study, we examine the impact of variations in gravity wave properties on the ice crystal number concentrations in the tropical tropopause layer (TTL). Analysis of quasi-Lagrangian superpressure balloon measurements from the Stratéole-2 campaign shows that high-frequency waves dominate the occurrence of relatively large vertical wind speeds. Both synthetic and observed time series of wave-driven vertical wind perturbations are used to drive ensembles of homogeneous freezing ice nucleation simulations. Reducing high-frequency variability from the time series reduces the occurrence of ice concentrations exceeding 1 cm^{-3}. In contrast, reducing the wave amplitudes at all frequencies simply shifts the entire frequency distribution of ice concentrations to lower values. We also derive analytic expressions for the ice concentration distribution and the mean ice concentration. The ice concentration statistics produced by these analytic expressions approximately reproduce the numerical results. Increasing high-frequency variability increases the likelihood of vertical wind speed changing from cooling to warming during a nucleation event. If wave frequencies approaching the Brunt-Väisälä frequency are included, this nucleation quenching effect has a significant influence on the mean ice concentration produced by homogeneous freezing. However, the increase in vertical wind speed amplitude associated with high-frequency waves dominates over the increased occurrence of quenching events, such that the overall impact of the high-frequency variability is to increase in ice concentrations. The observed natural variability in TTL gravity wave properties results in mean ice concentrations produced from homogeneous freezing ranging from about 0.8 to 4.9 cm^{-3}.

Plain Language Summary In this study, we examine the impact of variations in atmospheric waves on the formation of ice crystals in high-altitude tropical cirrus clouds. Analysis of measurements from high-altitude balloons is used to characterize the temperature and vertical wind perturbations driven by the waves. Waves with periods less than about 10 min dominate the occurrence of strong vertical winds in the upper troposphere. We use the balloon measurements, along with numerically generated wave perturbations to drive simulations of ice formation by spontaneous freezing of liquid aerosols. Reducing the amplitudes of rapid fluctuations substantially reduces the occurrences of very high ice concentrations. The observed natural variability in wave properties results in cirrus ice concentrations ranging from about 0.8 to 4.9 cm^{-3}.

1. Introduction

Cirrus clouds in the tropical upper troposphere have important impacts on the Earth's radiation budget and climate (Haladay & Stephens, 2009). In this study, we focus on cirrus formed in situ in the tropical tropopause layer (TTL). TTL cirrus affect the Earth's climate directly by scattering and absorbing radiation, and indirectly by regulating the amount of water that enters the stratosphere, which in turn has a significant effect on the radiation budget (Forster & Shine, 2002). Ice nucleation is the initial stage of cirrus cloud formation. The number concentration of ice crystals produced by an ice nucleation event represents the initial conditions for the cloud. The initial ice concentration is very important for the subsequent evolution and lifetime of the cirrus cloud (Jensen et al., 2025). For example, if relatively few ice crystals nucleate, they will be able to grow relatively large and sediment out of supersaturated layers quickly. As a result of the importance of cirrus ice number concentrations, a great deal of research has focused on understanding upper tropospheric ice nucleation processes.

Homogeneous freezing of supercooled aqueous aerosols is relatively well understood and known to occur in the TTL (Jensen et al., 2022). Numerous studies have shown that the number concentration of ice crystals produced

by homogeneous freezing increases rapidly with increasing cooling rate (e.g., Jensen & Toon, 1994; Kärcher & Lohmann, 2002). If solid or mixed-phase aerosols are present, heterogeneous nucleation may occur, in which case the ice concentration will typically be limited by the number of ice nucleating particles available. Here, we focus on wave impacts on homogeneous freezing in the TTL.

Cooling rates in the upper troposphere are dominated by gravity waves with spatial and temporal scales ranging from planetary waves with periods of weeks to high-frequency waves with frequencies approaching the Brunt-Väisälä frequency, N. Several recent studies have shown that gravity wave driven temperature oscillations regulate the number of ice crystals produced by homogeneous freezing in the TTL (Corcos et al., 2023; Dinh et al., 2016; Jensen et al., 2010, 2016; Jensen & Pfister, 2004; Spichtinger & Krämer, 2013). In general, these investigations have focused on the impacts of specific wave types or specific cases of measured wave-driven temperature fluctuations. Different approaches have been used to specify time series wave-drive vertical wind (or temperature) fluctuations in these studies. Here, we examine the impacts of observed variations in gravity wave properties on ice number concentrations produced by homogeneous freezing. We also compare the impacts of using different approaches for specifying the wave-driven mesoscale temperature fluctuations on frequency distributions and power spectra of vertical wind speed, as well as the resulting statistics of ice concentration produced by homogeneous freezing.

The paper is organized as follows: Section 2 presents observations of TTL wave properties and their variability. Section 3 provides a theoretical analysis and analytic expressions for wave impacts on ice concentrations produced by homogeneous freezing. Section 4 describes the approaches used for specifying mesoscale temperature fluctuations (MTF) driven by gravity waves. Section 5 describes the model used to simulate homogeneous freezing ice nucleation events. The results of our analysis are provided in Section 6, followed by a summary and discussion.

2. Observations of TTL Wave Properties

We use in situ observations of gravity waves from superpressure balloons flown during the Stratéole-2 first campaign. The data set consists of 8 balloon flights in the whole tropical band at altitudes of 18 and 20 km. All the balloons were carrying the Thermodynamical SENsor (Hertzog et al., 2007), which measured the pressure and temperature at 30 s time resolution. These measurements cover the entire spectrum of gravity waves. Further information about the campaign is provided in Corcos et al. (2021). Once at their equilibrium level, the superpressure balloons drift with the horizontal wind, providing observations in the intrinsic frame, a frame of reference moving with the wind (Massman, 1978; Vincent & Hertzog, 2014). These observations cover waves from the planetary scale to the Brunt-Väisälä frequency. We use a value of 0.0233 rad s^{-1} for N, which is typical for the TTL (Wilson et al., 2023). The air parcel vertical velocity and associated temperature variability generated by gravity waves are observed using the pressure measurements as in Corcos et al. (2021) and Podglajen, Hertzog, Plougonven, and Legras (2016). The pressure measurement has a higher precision (0.1 hPa, typically corresponding to 0.1 m at the balloon flight level) than the GPS altitude (precision of 1.5 m). The pressure measurement p'_{tot} is linked to the balloon vertical motion ζ'_b. More precisely, it is the sum of an Eulerian pressure disturbance p' and a Lagrangian contribution from the balloon motion in a background gradient of pressure:

$$p'_{\mathrm{tot}} = p' + \frac{d\bar{p}}{dz}\zeta'_b \tag{1}$$

where $\bar{p}$ is the mean pressure profile. The Lagrangian term dominates over the Eulerian one, and we neglect the latter here. We then consider that the balloon vertical motion, drifting on layers of iso density, is linearly linked to the air parcel's ζ'_θ (Massman, 1978; Nastrom, 1980; Vincent & Hertzog, 2014) on isentropic surfaces by:

$$\zeta'_b = \alpha\zeta'_\theta \tag{2}$$

with α of the order of 0.3 (Podglajen, Hertzog, Plougonven, & Žagar, 2016; Vincent & Hertzog, 2014). The corresponding change of temperature is deduced using an adiabatic transformation. This assumption is valid as long as the balloon keeps an isopycnal behavior. However, the assumption becomes questionable for intrinsic frequencies close to N for two reasons. First, the balloons undergo a neutral oscillation around their equilibrium

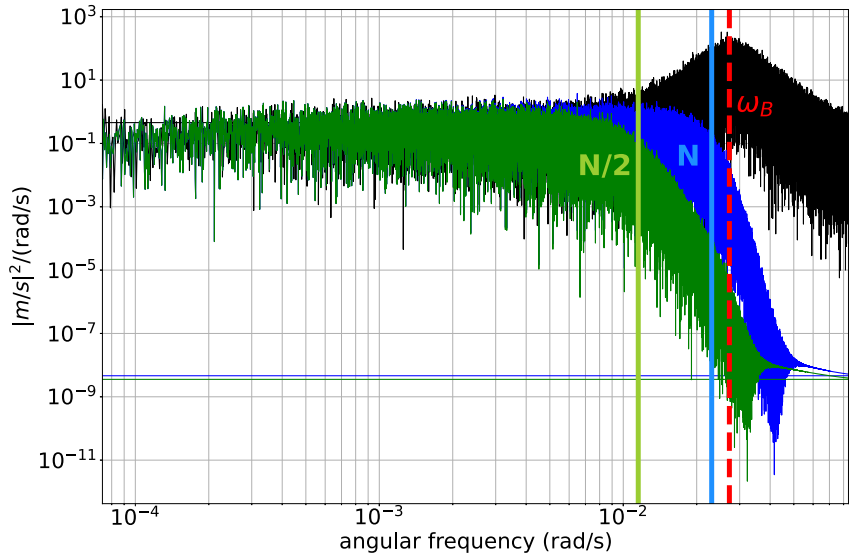

Figure 1. Example of power spectra of vertical wind for one of the Stratéole-2 flights (black curve) and filtered observations with periods between $2\pi/N$ and one day (blue curve) and $4\pi/N$ and one day (green curve). ω_b represents the balloons neutral oscillations central frequency.

level, at a typical period of 2–3 min. Second, the inertia of the balloons creates a slight departure from their isopycnic behavior at these higher frequencies, inducing a phase shift (Boccara et al., 2008) that can be problematic for derivation of typical wave characteristics (Podglajen, Hertzog, Plougonven, & Žagar, 2016; Vincent & Hertzog, 2014). However, these limitations do not affect our calculation of the vertical wind and derived variance.

Different filters can be used in order to select the range of periods corresponding to gravity waves in the tropical band. We use a Bessel filter to remove the periods longer than a day, and chose N and $N/2$ as the high-frequency cut off. Using these two values allows us to look at the impact of the highest frequency gravity waves on the vertical wind distribution. For the higher frequency cut-off N, we carefully filtered out the peak of power spectra corresponding to the balloons' neutral oscillations. While we can not say that this artifact was completely removed, we greatly limited its impacts on our analysis. The result is highlighted by Figure 1. Note that by using a cutoff of N/2 (or even N), we are removing variability near N. Past studies have shown that vertical wind speed power spectra can exhibit a local maximum near the Brunt-Väisälä frequency (Kottayil et al., 2024). We show here that this uncertainty in wave amplitudes near N is important for ice nucleation in the TTL.

The upper tropospheric variability of vertical wind is mostly carried by the waves with periods between 5 and 10 min, as shown by the nearly flat spectrum of the vertical wind in Figure 1. Time series also shows the presence of sporadic events that can be an order of magnitude higher than the baseline (not shown). These large-amplitude events contribute greatly to the width of the distribution of vertical velocities when higher frequencies are not filtered out. Figure 2 shows the importance of frequencies between $N/2$ and N for an accurate representation of the vertical wind variability.

Convection is the main source of gravity waves in the tropical band. These gravity waves are less intermittent than in higher latitudes as convection is ubiquitous in the tropics. Superpressure balloons have highlighted the variability of the gravity wave activity in the tropical lowermost stratosphere in terms of distance from their source. Following the method of Corcos et al. (2021), Figure 3 shows the evolution of vertical wind standard deviation, from waves with periods between 15 min and a day, with distance to the nearest convective cell from the observations. The standard deviation exhibits a rapid decay in the vicinity of convective cells and a more stable value beyond 200 km of 6.5 cm/s. The width of the boxplots highlights the variability of the vertical wind in the upper TTL. Balloons were flying more than 300 km from a convective cell the majority of the time.

For the purpose of assessing the variability in wave-driven vertical wind speed frequency distributions, we subdivide the N-filtered Stratéole-2 balloon time series into 5-day segments. We experimented with different

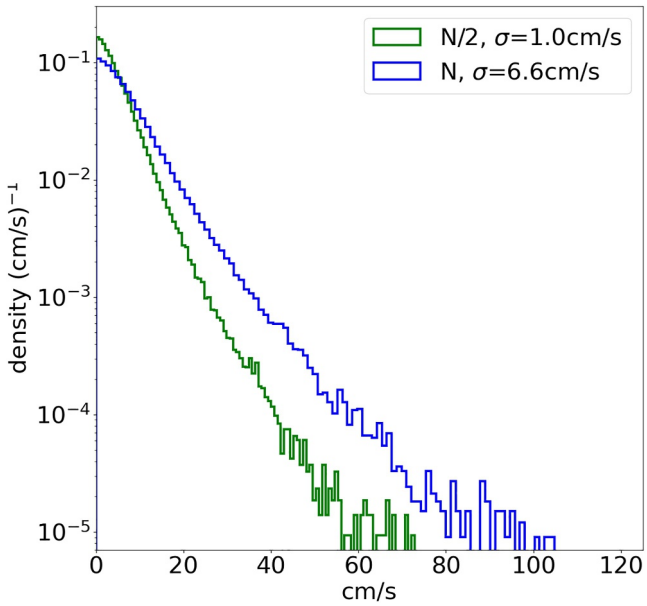

Figure 2. Probability density functions of vertical wind speed for the filtered observations with period between one day and $1/N$ (blue curve) or $2/N$ (green curve).

segment lengths and chose 5 days as sufficiently long to provide an adequate statistical sample. Figure 4 shows the variability in vertical wind speed and temperature standard deviations (σ_w and σ_T, respectively) from the 5-day TTL and stratosphere (STR) balloon time series segments. Vertical wind speed standard deviations in the TTL range from about 10 to 24 cm s^{-1}, whereas in the stratosphere, σ_w shows slightly greater variability, with values ranging from 8 to 28 cm s^{-1}. The average value for each balloon flight is also shown on the figure and is always higher at the TTL flights levels than at the STR levels. This tendency might come from filtering from wind shear and breaking of some waves before reaching the STR flight level. The temperature standard deviations range from 0.8K to 2K in the TTL and 0.7K–1.6K in the lower stratosphere. These ranges are consistent with the results from a similar analysis using the Project Loon superpressure balloons (Schoeberl et al., 2017).

Vertical wind speeds have also been measured in the TTL with high-altitude aircraft. The Airborne Tropical Tropopause Experiment (ATTREX) included extensive TTL vertical wind measurements over the Pacific (Jensen et al., 2017). Vertical wind speeds were measured with the Meteorological Measurement System (MMS; Scott et al., 1990). Wind speeds are determined by combining the aircraft attitude information with measurements from differential pressure sensors on the aircraft fuselage. The precision of the MMS vertical wind speed measurement is 5 cm s^{-1}.

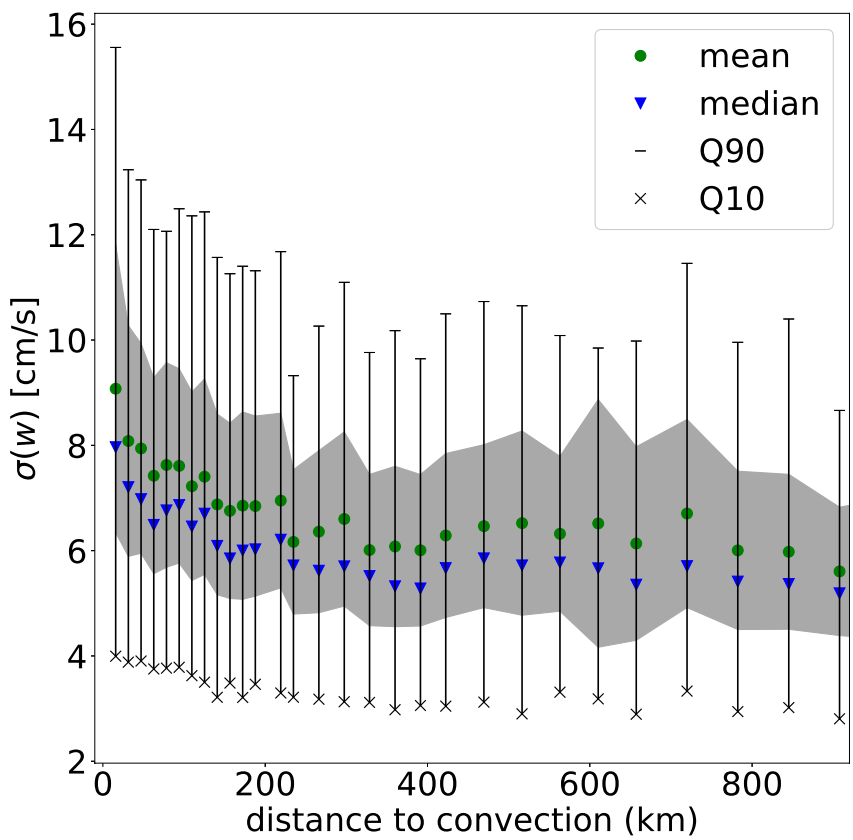

Figure 3. Boxplots of vertical wind standard deviation as a distance to the nearest convective cell, for waves with periods between 15 min and one day. Note that elsewhere in the paper we include higher-frequency variability approaching N. Gray shading corresponds to the standard deviation of the measurements.

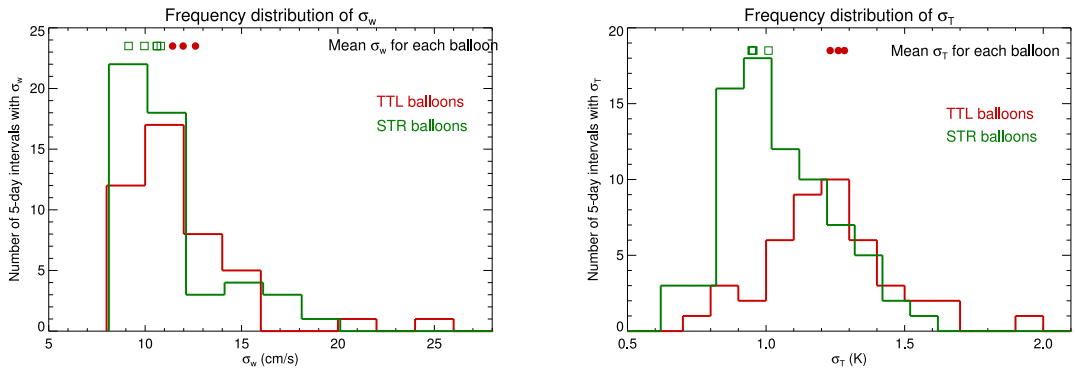

Figure 4. Frequency distributions of vertical wind speed (left panel) and temperature perturbation (right panel) standard deviations based on 5-day segments along the Stratéole-2 N-filtered balloon paths.

Figure 5 compares frequency distribution of vertical wind speed from the ATTREX MMS measurements in the TTL with one of the Stratéole-2 TTL balloon flights. (The vertical wind speed standard deviation for this balloon (TTL3) is 11.97 cm s^{-1}.) Note that the vertical wind speed distributions are exponential, consistent with Podglajen, Hertzog, Plougonven, and Legras (2016) and Kärcher and Podglajen (2019) (hereinafter KP19). Both the overall distribution including all of the ATTREX data (black curve), and the range corresponding to individual aircraft flights (gray shading) are shown. The vertical winds inferred from the Stratéole-2 measurements are somewhat lower than the average vertical winds measured during ATTREX. However, the ATTREX flights occurred in the western Pacific during late Boreal wintertime in a highly convective environment. Also, the 0.05 m s^{-1} precision of the MMS measurement implies that noise may have contributed somewhat to the breadth of the vertical wind speed distribution. Another possibility is that the ATTREX measurements included high-frequency variability (near *N*) that has been filtered out of the balloon time series.

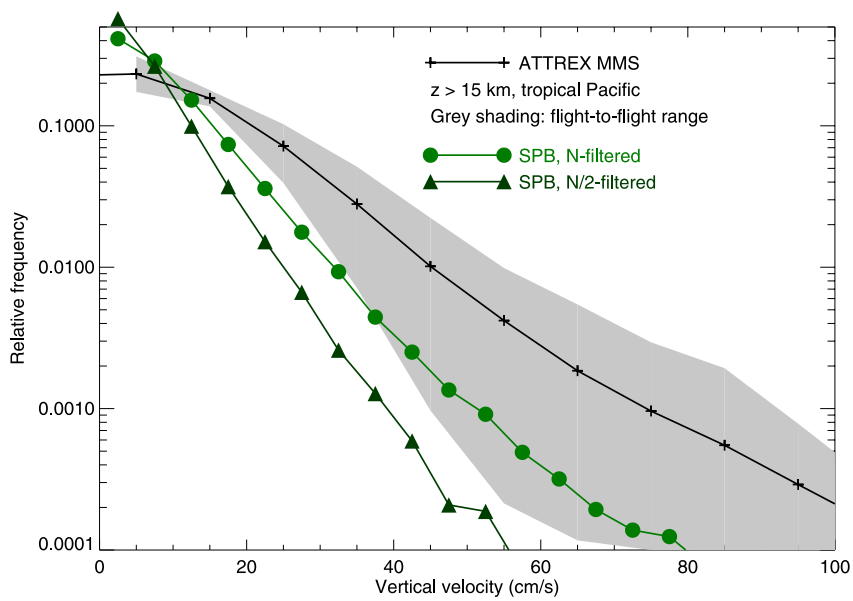

Figure 5. The frequency distributions of vertical wind speed from one of the Stratéole-2 N- and N/2-filtered TTL balloon time series (green and dark green curves curve) are compared to aircraft measurements made with the meteorological measurement system in the TTL during the ATTREX campaign. The solid black curve includes all ATTREX TTL data, and the gray shaded region shows the range in frequency distributions from individual flights.

3. Analytic Expressions for the Statistics of Nucleated Ice Concentrations

Our ensembles of numerical simulations presented below produce frequency distributions of homogeneously nucleated ice crystal number concentrations. We compare those with a simple analytical estimate, that is, based on the observed statistics of wave-driven vertical wind speed fluctuations and on cloud physics theory (Kärcher & Lohmann, 2002).

The probability density function for the vertical wind speed perturbation (w') is given by

$$\frac{dP}{dw'} = \frac{1}{w_m} e^{-w'/w_m}, \tag{3}$$

with the mean value $w_m = \sigma_w/\sqrt{2}$. Nucleated ice concentration (n) exhibits a power law dependence on updraft speeds in the mesoscale regime:

$$n(w') = n_1 \left(\frac{w'}{w_1}\right)^{3/2}. \tag{4}$$

We only consider updrafts ($w' \geq 0$). Slow ($\ll w_m$) contributions unrelated to gravity wave activity have little impact on the nucleated ice concentration. Based on our numerical homogeneous freezing simulations described below, we specify w_1 and n_1 as 10 cm s^{-1} and 1.2 cm^{-3}, respectively. In other words, the numerical model indicates that a homogeneous freezing event forced by an updraft speed of 10 cm s^{-1} produces 1.2 cm^{-3} ice crystals. This simulation was run at a pressure of 100 hPa and a temperature of 190K.

Taken together, the instantaneous statistic of nucleated ice numbers,

$$\frac{dP}{dn} = \frac{dP/dw'}{dn/dw'}, \tag{5}$$

is given by

$$x\frac{dP}{dx} = \frac{2}{3} x^{2/3} e^{-x^{2/3}}, \qquad x = \frac{n}{n(w_m)}. \tag{6}$$

We compute the mean nucleated ice concentration as the area under this distribution:

$$n_m = n(w_m) \int_0^\infty x^{3/2} e^{-x} dx = \frac{3}{4}\sqrt{\pi}\, n(w_m), \tag{7}$$

showing that averaging over individual wave-induced fluctuations slightly increases n above the value evaluated at the mean updraft speed.

4. Approaches Used for Generating Synthetic Mesoscale Temperature Fluctuations

Various approaches have been used to derive time series of vertical wind and temperature fluctuations for use in ice nucleation simulations. These approaches include superposition of individual sinusoidal functions with an appropriate range of frequencies and amplitudes (Jensen & Pfister, 2004), statistical models constrained by the Stratéole-2 superpressure balloon measurements (Kärcher & Podglajen, 2019; Podglajen, Hertzog, Plougonven, & Legras, 2016), and direct use of the time series from the balloon flights (Corcos et al., 2023; Dinh et al., 2016; Jensen et al., 2016). Here, we briefly describe the different methods and compare the resulting statistic of vertical wind speeds and resulting ice concentrations.

4.1. Fourier Series Approach

The approach used by Jensen and Pfister (2004) (hereafter referred to as JP04) and several subsequent modeling studies (e.g., Ueyama et al., 2015, 2018) consists of a Fourier series in time with 70 frequencies ranging from

3.2×10^{-7} to 10^{-3} Hz. Here, we have extended the Fourier series to 90 frequencies such that we include components approaching the Brunt-Väisälä frequency. A base vertical wind speed perturbation amplitude for a wave frequency of 1 day^{-1} is chosen, and amplitudes for higher frequencies are specified using a -2 power law. We have adjusted the base amplitude such that the standard deviation of vertical wind speed and temperature approximately match those indicated by the Stratéole-2 measurements. For each frequency, the wave phase is chosen at random, and a vertical wavelength is chosen randomly in the 1.5–5 km range. This vertical wavelength range assumption will exclude horizontally short waves with long vertical wavelengths. However, as discussed by Jensen and Pfister (2004), the impact of these waves on the temperature field in the TTL is probably small. Large ensembles of ice nucleation simulations are generated by choosing different random phases and vertical wavelengths. The original scheme included low-frequency waves (such as planetary waves). Here, we focus on waves with frequencies higher than 1 day^{-1} since the low-frequency waves have a negligible impact on statistics of ice concentrations.

In summary, the vertical wind speed perturbation at each time step is calculated as a sum of the individual frequency components:

$$\Delta w_j = w_{amp_j} \sin\left(\hat{\omega} t + mz + \phi_j\right) \tag{8}$$

and the sum is taken over the frequencies ranging from 1/day up to the Brunt-Väisälä frequency.

4.2. Statistical Model Approach

The other approach we use for generating synthetic time series of wave-driven fluctuations is based on Kärcher and Podglajen (2019) KP19 and involves modeling a wave background state that is no longer dominated by local wave sources. Figure 3 supports (in terms of σ_w) the existence of background conditions that appear to be typically reached at distances >200 km away from tropical deep convection. A similar conclusion was reached by Corcos et al. (2021) based on σ_T measurements.

In the KP19 approach, all intrinsic wave frequencies in the mesoscale range, from N to the inertial frequency (f), contribute equally to the power spectrum of vertical wind speed fluctuations (w'). In the time series, consecutive $w'(t)$-values are assumed to be fully correlated over a time $\tau = 1/N$, after which their magnitude and possibly sign change abruptly as they are sampled randomly from a two-sided exponential distribution (Laplacian) for given σ_w:

$$\frac{dP}{dw'} = \frac{1}{2b} \exp\left(-\frac{|w'|}{b}\right), \tag{9}$$

with the scale parameter $b = \sigma_w/\sqrt{2}$. This distribution provides a good fit to the measured fluctuations (Podglajen, Hertzog, Plougonven, & Legras, 2016).

The stochastic model for mesoscale temperature fluctuations (T') is based on the adiabatic cooling/heating rates resulting from the w' time series and includes a low-frequency damping to prevent the associated standard deviation σ_T from diverging. As we do not make direct use of $T'(t)$, we do not discuss damped MTF any further, but note that both σ_T and the corresponding standard deviation of cooling/heating rates averaged over an ensemble of MTF paths (σ_κ) are related to the geometric mean wave frequency (ν) via $\nu = \sqrt{fN} = \sigma_\kappa/\sigma_T$, within about 30% in agreement with superpressure balloon (SPB) data.

The KP19 model can be constrained by the input parameters σ_T, f, and N. In addition, an input value for σ_w is needed to sample w'-values. Noting that σ_w differs from the simulated value of σ_κ/Γ due to the damping, we introduce a correction factor (c) to obtain σ_w from

$$\sigma_w = c_1 \frac{\sigma_\kappa}{\Gamma} = \frac{c_1}{\Gamma} \sigma_T \nu\,, \tag{10}$$

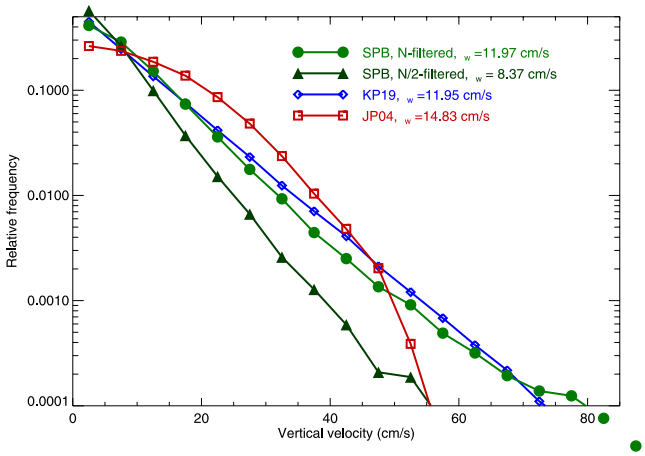

Figure 6. The frequency distribution of vertical wind speed from one of the Stratéole-2 TTL N- and N/2-filtered balloon time series (green and dark green curve) are compared with synthetic frequency distributions derived with the JP04 approach (red curve) and the KP19 approach (blue curve).

whereby we determined $c_1 = 1.41$ by running ensemble simulations with different input parameters, and Γ is the adiabatic lapse rate. This approach results in MTF paths in line with SPB data and with self-consistent input values for σ_T and σ_w.

To address the consequences for ice nucleation statistics of filtering out high wave frequencies in the w' time series, we substitute N by a lower frequency (N/z) with the filtering factor $N/f \geq z \geq 1$. If we remove the part of the wave frequency spectrum between N and N/z leaving σT constant, then ν and thus σ_w decreases $\propto 1/\sqrt{z}$.

With the above relationships (Section 3), we cast the relationship for the mean nucleated ice number concentration (n_m) into the form

$$n_m = cn_1\left(\frac{W}{w_1}\right)^{3/2}, \quad c = \frac{3}{4}\sqrt{\pi}\left(\frac{c_1}{\sqrt{2}}\right)^{3/2} = 1.3234, \quad W = \frac{\sigma_T \nu}{\Gamma}, \qquad (11)$$

where W is an effective updraft speed that scales with the wave-induced mean cooling rate $(\sigma_T \nu)$.

4.3. Direct Use of the Stratéole-2 Superpressure Balloon Measurements

Direct use of the N-filtered time series of vertical wind speed from the Stratéole-2 balloon measurements is straightforward. The time resolution of the Stratéole-2 data is 30 s, and we use linear interpolation to obtain the vertical wind speed at the simulation time. As discussed below, the time step used in the simulations is 0.1 s. In order to produce ensembles of homogeneous freezing simulations, we initialize each simulation at different times along the Stratéole-2 data time series. Specifically, we initialize the first simulation at the beginning of a balloon time series, initialize the next simulation 5 min after the beginning of the balloon time series, and so on. Each simulated nucleation event will therefore have a unique vertical wind speed (cooling rate) at the time nucleation occurs.

4.4. Comparison of Vertical Wind Speed Statistics From Different Approaches

The vertical wind speed frequency distributions corresponding to these approaches for generating synthetic mesoscale temperature fluctuations are compared to the corresponding frequency distribution from one of the Stratéole-2 TTL balloon flights in Figure 6. The KP19 approach produces vertical wind speeds that are statistically very similar to the balloon measurements since this approach was developed using the fluctuation statistical properties indicated by the measurements. The JP04 approach produces a vertical wind speed frequency distribution with distinctly different curvature. The distribution is Gaussian, which is expected since we are sampling randomly from a harmonic time series. However, the wind speed standard deviations are similar to the other methods since we used the Stratéole-2 measurements to constrain the base amplitude. Below, we compare the statistics of ice number concentration produced by homogeneous freezing using time series of vertical wind speed fluctuation generated with these different approaches.

Vertical wind speed power spectra from the Stratéole-2 measurements and the different approaches for generating synthetic time series are shown in Figure 7. The spectra are approximately flat for periods between 1 day and $2\pi/N$, as expected. The JP04 scheme excludes any contribution at frequencies beyond N by design. The Bessel filter used for the SPB time series rolls off sharply beyond N, but there may be a slight contribution from variability with periods between 3 and 5 min.

5. Model for Simulation of Homogeneous Freezing Ice Nucleation Events

Our objective here is to run ensembles of homogeneous freezing ice nucleation simulations to investigate the relationships between the properties of wave-driven vertical wind speed fluctuations and the statistics of ice number concentration. For this purpose, we run parcel simulations with the Community Aerosol and Radiation Model for Atmospheres (CARMA) bin microphysics model (Bardeen et al., 2008; Jensen et al., 2002; Toon

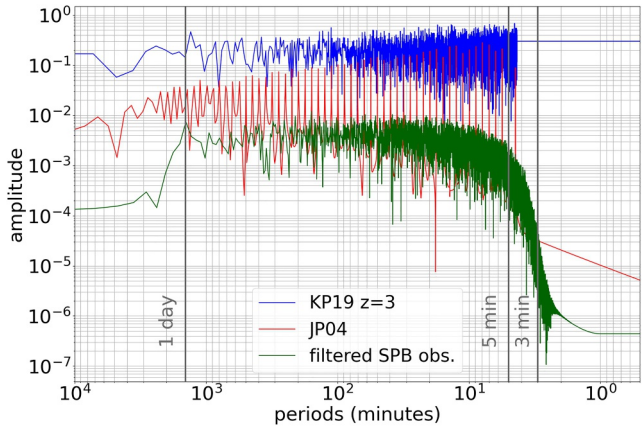

Figure 7. Vertical wind speed power spectra are shown based on the filtered Stratéole-2 time series (green), the JP04 synthetic time series (red), and the KP19 synthetic time series with $z = 2$ (blue). For clarity, the JP04 spectrum is shifted down by a factor of 10, and the Stratéole-2 spectrum is shifted down by a factor of 100.

et al., 1988). The model is set up with two particle groups: aqueous sulfate aerosols and ice crystals. We use 80 particle size bins, spanning a size range of 0.01–10 μm for the aerosol group and 0.01–240 μm for the ice crystal group. The ratios of particle volumes in successive bins are 1.3 and 1.6 for the aerosol and ice crystal groups, respectively. For simplicity, we assume the ice crystals are equivalent-mass spheres. This assumption is reasonable given the small ice crystal sizes in TTL cirrus, particularly since we are only simulating the ice nucleation stage of the cloud lifecycle, and we terminate the simulations before the ice crystals have a chance to grow larger than about 10 μm. Currently available observations do not provide information about the habits of TTL cirrus ice crystals smaller than about 40 μm (Woods et al., 2018).

We specify a log-normal initial aerosol size distribution, with total number concentration $N = 1000$ cm^{-3}, mode radius $r_0 = 0.1$ μm, and standard deviation $\sigma = 1.6$. The number concentration of ice crystals produced by homogeneous freezing is relatively insensitive to the aerosol size distribution; ice concentrations are primarily controlled by cooling rate (vertical wind speed; Kärcher & Lohmann, 2002). For calculation of the temperature- and supersaturation-dependent homogeneous freezing rate, we use the expressions provided by Koop et al. (2000). We have adjusted the water activity by a multiplicative factor such that the ice supersaturation threshold for homogeneous freezing agrees with higher values (ice supersaturation ≃110% at 190K) indicated by recent laboratory experiments (Schneider et al., 2021).

Each simulation is initialized with a temperature of 190K, a pressure of 100 hPa, and an ice supersaturation just below the threshold for homogeneous freezing. TTL temperatures can be somewhat colder or considerably warmer than 190K, but we are not attempting to explore the temperature dependence here. We force the simulations with the time series of vertical wind speed from either the superpressure balloon measurements or one of the synthetic approaches. The model time step is 0.1 s. We have confirmed that using smaller time steps does not change the results. We terminate each simulation after the ice nucleation event is complete; specifically, we end the simulations if the ice number concentration is greater than 0.001 cm^{-3} and the ice supersaturation has dropped below 20%. For each ensemble we run approximately 40,000 individual simulations in order to produce smooth frequency distributions of ice number concentration that capture the low-frequency tails of the distributions.

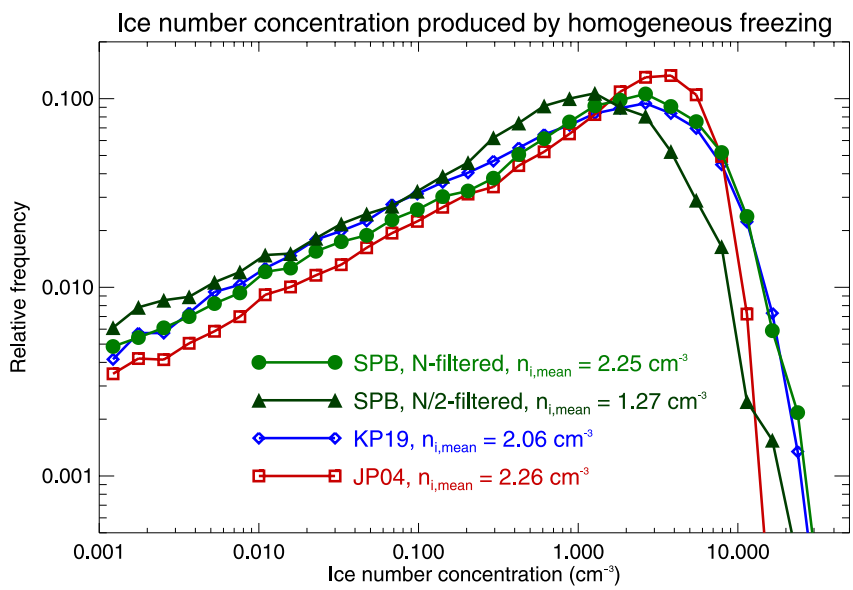

Figure 8. The frequency distribution of ice number concentration (dP/dlog$n$) produced by homogeneous freezing. The different curves correspond to ensembles of simulations using the Stratéole-2 balloon time series directly (green and dark green curves), the JP04 approach (red curve), and the KP19 approach (blue curve).

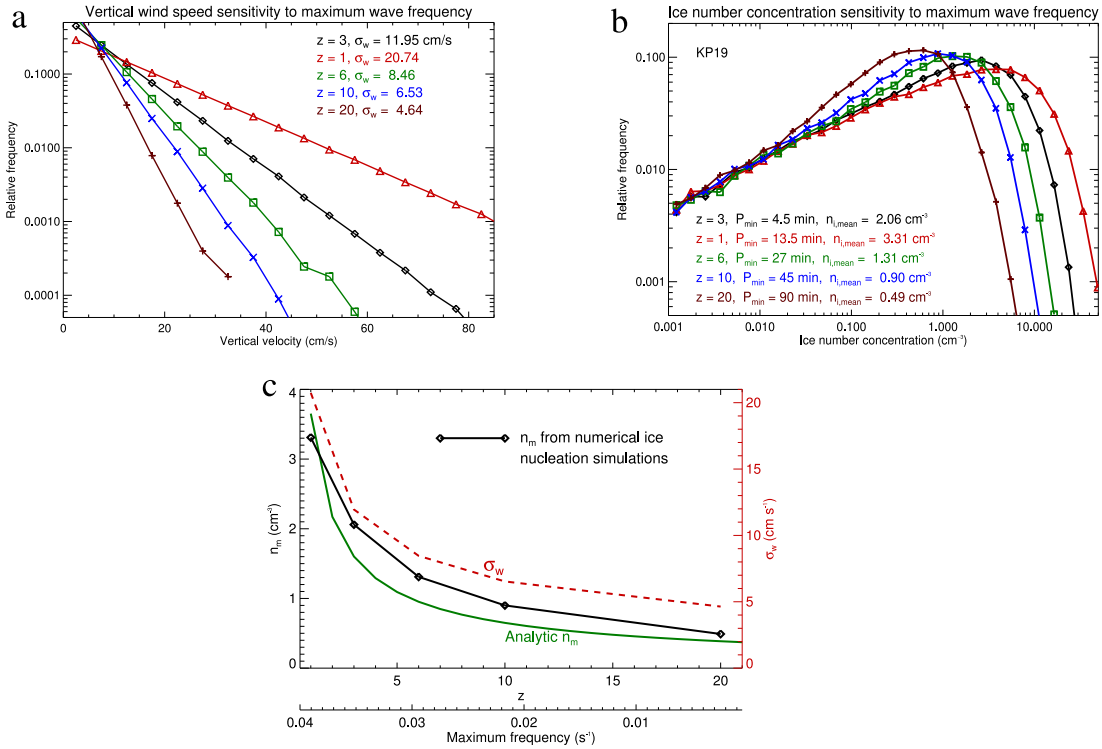

Figure 9. The impacts of truncating the highest frequency variability in vertical wind speed on frequency distributions of vertical wind speed (a) and ice number concentrations produced by homogeneous freezing (b). Panel (c) the mean ice number concentration produced by homogeneous freezing (black curve) is plotted versus z (or, equivalently, versus the maximum frequency of vertical wind speed variability). The green curve shows the corresponding result from the analytic expression (Equation 9). The red dashed curve shows the reduction of σ_w with increasing z. See text for discussion.

6. Results

We begin by comparing the frequency distributions of ice number concentration generated by ensembles of simulations using the Stratéole-2 balloon time series and the two synthetic approaches (see Figure 8). In general, the simulated ice concentration frequency distributions are quite similar. As expected, using the N/2-filtered balloon time series results in lower ice concentrations. Removing frequencies above N/2 substantially reduces the occurrence of ice concentrations greater than 1 cm^{-3}. Despite the different shape of the JP04 vertical wind speed frequency distribution, the resulting ice concentration frequency distribution is similar to that produced by using either the Stratéole-2 data directly or the KP19 approach.

Next, we use the KP19 approach with different values of the filtering parameter z to investigate the impacts of truncating the highest frequency variability on vertical wind speed and ice number concentration statistics. Figure 2 highlighted the importance of waves with intrinsic frequencies between $N/2$ and N for the tail of the vertical wind speed distribution. Furthermore, Corcos et al. (2021) documented the variability in the presence of high frequency waves in the TTL. Figure 9 shows the vertical wind speed and ice concentration frequency distributions from ensembles of simulations with z ranging from 1 to 20, which corresponds to maximum frequencies ranging from $N = 0.0233$ rad s^{-1} to about 1×10^{-3} rad s^{-1}. Note that z set to 10, we get $\sigma_w = 6.5$ cm s^{-1}, which is consistent with the value derived from the balloon measurements far from convection (Figure 3). As expected, the high frequency waves dominate the occurrence of the largest vertical wind speeds, and the frequency distribution of vertical wind speed narrows considerably when the highest-frequency variability is eliminated. For example, truncating waves with periods less than about 45 min (z =10) results in about a factor of 2 decrease in the vertical wind speed standard deviation compared to the baseline z =3 case with variability at periods down to about 4.5 min (= N). The ice number concentration frequency distributions show that these high frequency waves also dominate the occurrence of the highest ice concentrations. Truncating waves with periods less than 45 min eliminates ice concentrations greater than a few per cm^3 and reduces the mean ice concentration

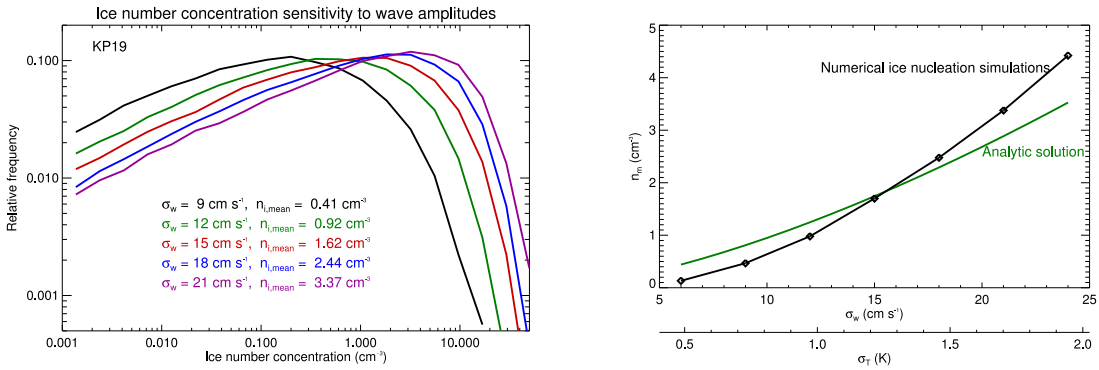

Figure 10. (a) The dependence of the ice number concentration frequency distribution on the overall amplitude of vertical wind speed variability is shown. The solid curves show results from ensembles of homogeneous freezing simulations. Panel (b) The mean ice number concentration is plotted versus the vertical wind speed standard deviation (black curve). The green curve shows the corresponding dependence indicated by the analytic expression (Equation 9). The lower axis shows the temperature standard deviation.

by more than a factor of 2. We note that ice concentrations exceeding 10 cm^{-3} do occur in TTL cirrus (Jensen et al., 2022). Similar results (not shown) were obtained using the JP04 approach and simply omitting the highest frequencies from the Fourier series. The dependencies of σ_w and mean ice number concentration on z are shown in Figure 9c. Mean ice concentration decreases from about 2 cm^{-3} to 0.5 cm^{-3} as the maximum frequency decreases from 0.04 to 0.002 s^{-1}.

As shown in Figure 4, the Stratéole-2 measurements indicate considerable variability in wave amplitudes (as quantified by the vertical wind speed and temperature standard deviations). Figure 10 shows the impacts on ice number concentrations of varying the MTF amplitude over the range indicated by the observations. As expected, the ice concentration frequency distributions shift substantially toward higher ice concentrations when the overall MTF amplitudes increase. The mean ice concentration increases from about 0.41 cm^{-3} to 3.4 cm^{-3} as σ_w increases from 9 to 21 cm s^{-1} (right panel in Figure 10).

Ice number concentration frequency distributions calculated with the analytic expression (Equation 6) are compared with the numerical results in Figure 11 for two different values of z. We have constrained the analytic distributions such that they have the same mean ice number concentration as the corresponding numerical

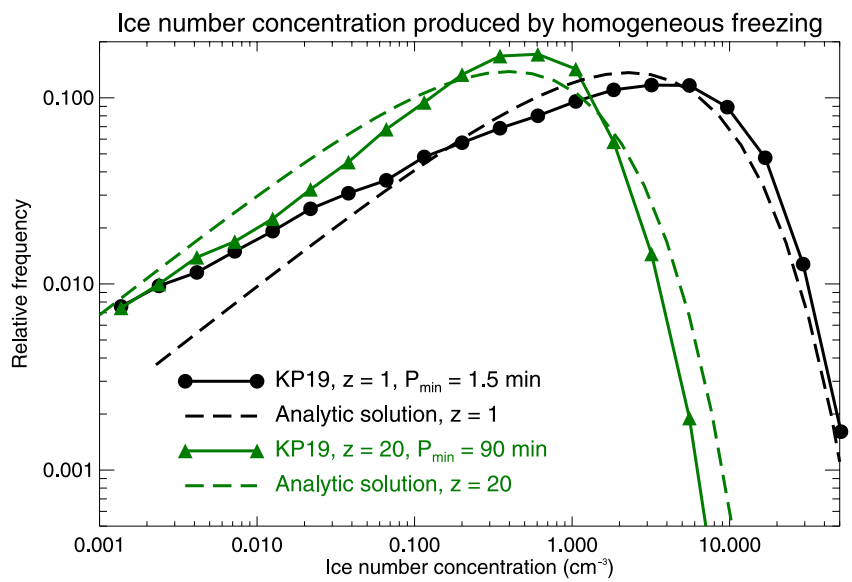

Figure 11. Ice number concentrations are shown for $z = 1$ (black curves) and $z = 20$ (green curves). Solid curves show the numerical results, and dashed curves show the analytic solution (see Section 3).

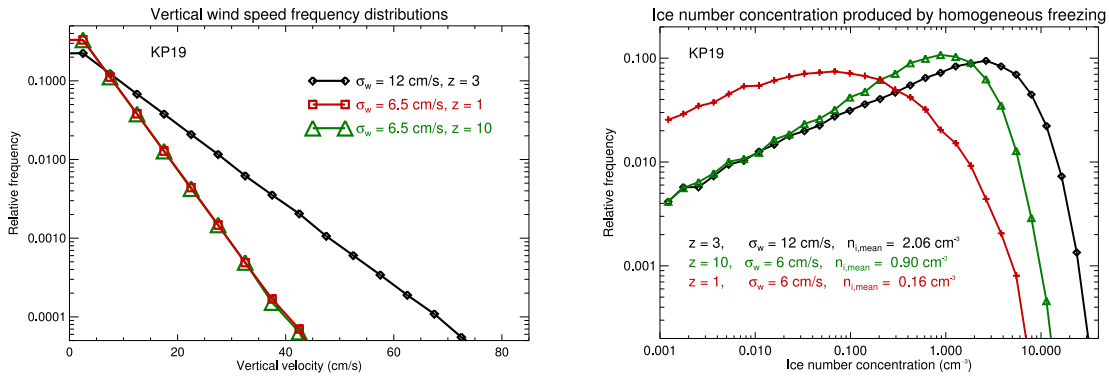

Figure 12. Vertical wind speed frequency distributions (a) and ice number concentration frequency distributions (b) are shown for three cases: Baseline wave properties (black curves), High-frequency variability removed by increasing z to 10 (green curves), and variability at all frequencies reduced by a factor of 2 with z =1 (red curves).

ensembles. In general, the analytic solution agrees well with the numerical results. In the case of $z = 1$, which includes high-frequency variability, the analytic solution has fewer occurrences of low ice concentrations (less than about 0.1 cm^{-3}) than indicated by the numerical results. We hypothesize that this discrepancy is a result of the quenching effect when the temperature tendency switches from cooling to warming during a nucleation event (Dinh et al., 2016; Jensen et al., 2010, 2016; Spichtinger & Krämer, 2013). The quenching process can lead to increased frequency of low ice concentrations. This effect is included in the numerical results, but not in the analytic derivation. This hypothesis is consistent with the fact that in the case of $z = 20$, which excludes high frequency variability, the analytic solution is closer to the numerical results at the low end of the ice concentration distribution.

Figures 9c and 10b also show results from the analytic expression derived in Section 3 for mean ice number concentration (Equation 9) for comparison with the numerical results. The analytic expression for mean ice concentration reproduces the numerically derived dependencies on z and σ_w. The general agreement between the numerical results and the analytic expressions (which do not include the nucleation quenching effect) shows that the quenching effect does not dominate the mean ice concentration produced by wave-driven temperature variability.

An additional issue we address here is the relative impact of truncating high frequency variability versus decreasing the vertical wind speed variability at all frequencies. In the example shown in Figure 12, we have chosen the value of $z = 10$ such that the vertical wind speed standard deviation is reduced by a factor of 2 compared to the baseline case with $z = 3$. We compare this with a set of simulations with z =1, but with the overall amplitude decreased by a factor of 2. Figure 12a shows that with z =10, the vertical wind speed frequency distribution is essentially identical to the distribution produced by simply reducing the wave amplitudes at all frequencies by a factor of 2. However, the ice number concentration frequency distributions (Figure 12b) are quite different. Using the time series with overall vertical wind speed variability reduced results in considerably lower ice concentrations than using the time series with only high frequencies removed. Removing only the high-frequency vertical wind speed variability primarily just eliminates the highest ice concentrations produced by homogeneous freezing (ice concentrations greater than about 3 cm^{-3} in this example), whereas reducing amplitudes across all frequencies shifts the entire ice concentration frequency distribution toward lower concentrations.

In order to evaluate this issue further, we generated statistics of vertical wind speed during the homogeneous freezing nucleation events. Specifically, we ran 40,000 ice nucleation simulations for each case and recorded the vertical wind speeds and ice concentrations when the ice concentration was increasing at a rate greater than $dn_{ice}/dt_{\min} = 10^{-4}$ and 10^{-2} cm^{-3} s^{-1}. For a typical nucleation event duration of at least 1 min, these rates would correspond to nucleation events producing more than about 0.006 cm^{-3} and 0.6 cm^{-3} ice crystals, respectively. The resulting frequency distributions of vertical wind speed for the $\sigma_w = 6$ cm s^{-1} and z =1 versus z =10 cases are shown in Figure 13. The vertical wind speeds during nucleation events are considerably higher in the $z = 10$ case. Further, in the $z = 1$ case, the vertical wind speed is sometimes negative while ice nucleation is occurring.

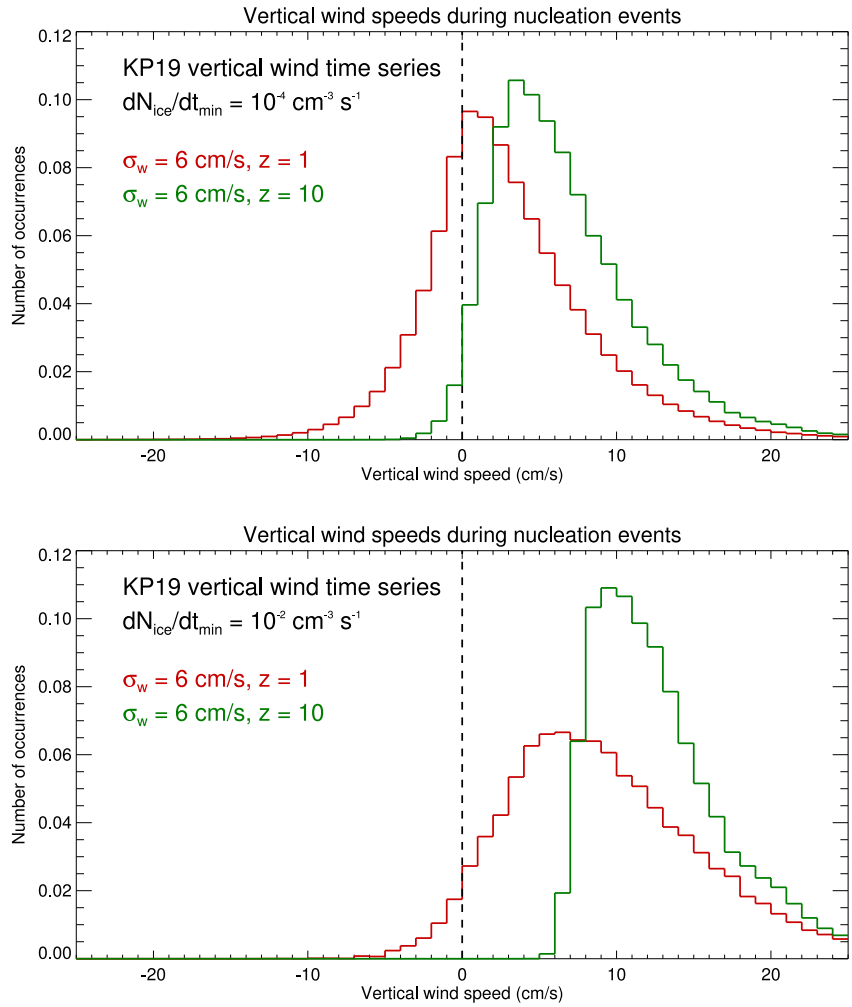

Figure 13. Vertical wind speed frequency distributions during homogeneous freezing nucleation events. Top panel: nucleation rates greater than 10^{-4} cm^{-3} s^{-1}. Bottom panel: nucleation rates greater than 10^{-2} cm^{-3} s^{-1}. Red curves: ensemble of nucleation simulations using the KP19 vertical wind speed time series with $\sigma_w = 6$ cm s^{-1} and $z = 1$; green curves: ensemble with $z = 10$.

The vertical wind speeds during nucleation increase when we increase the minimum nucleation rate, as expected. As noted above, the primary difference between the time series of vertical winds used in the two cases shown in Figure 12 is the reduced high-frequency variability in the $z = 10$ case. We hypothesize that the lower ice concentrations in the $z = 1$ case result from more frequent occurrence of nucleation quenching associated with reversals of the vertical wind speed from positive to negative during the nucleation events. With the reduced high-frequency variability in the $z = 10$ case, the nucleation quenching occurs relatively infrequently.

As an additional diagnostic, we examined the nucleation events in these ensembles and noted how often the vertical wind speed changes from positive to negative while the ice concentration is between 5% and 95% of its maximum value (i.e., during the nucleation events.) For the $z = 10$ case, only 17% of the nucleation events had vertical wind speed sign changes, whereas in the $\sigma_w = 6$ cm s^{-1}, $z = 1$ ensemble, 92% of the nucleation events had w reversals. We conclude that high-frequency variability in vertical wind speed can increase ice concentrations produced by homogeneous freezing by increasing the occurrence of strong updrafts, but it can also decrease ice concentrations by increasing the frequency of quenching events.

The importance of the quenching process can be seen even more clearly by examining the ice concentration frequency distributions for nucleation events with and without vertical wind speed reversals during the nucleation events (Figure 14). In the ensemble with $z = 10$, nucleation events without quenching dominate for cases with ice

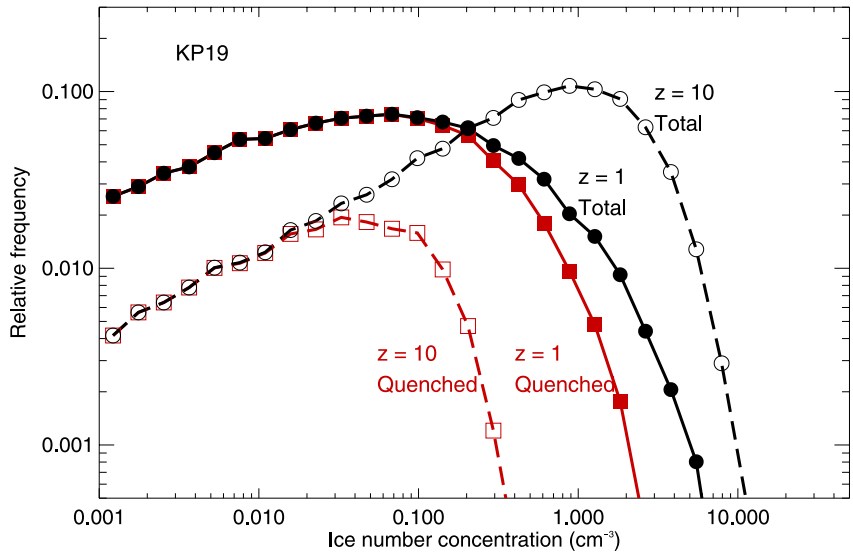

Figure 14. Ice number concentration frequency distributions are shown from the ensembles of simulations using the KP19 time series with $z = 1$ and σ_w reduced from 12 to 6 cm s^{-1} (solid curves with filled symbols), and with z increased from 1 to 10 (dashed curves with open symbols). Black curves include all nucleation simulations, whereas the red curves only include simulations with a vertical wind speed reversal (i.e., quenched nucleation events).

concentration exceeding about 0.1 cm^{-3}, whereas most nucleation events producing lower ice concentrations were quenched. In the $\sigma_w = 6$ cm s^{-1}, $z = 1$ case, most nucleation events are quenched overall, and unquenched events only contribute significantly when the nucleated ice concentration is greater than 1 cm^{-3}. Part of the reason this ensemble has such a large fraction of quenched events is the relatively low vertical wind speed amplitudes. With weaker vertical winds, the nucleation events last longer, providing more opportunity for a quenching event to occur.

We note here that Jensen et al. (2016) also used ensembles of homogeneous freezing simulations to investigate the quenching effect. They concluded that the quenching process had little impact on the ice concentration frequency distribution. However, they were using the old version of the JP04 parameterization. As noted above, for this study, we have extended the Fourier series in the JP04 scheme up to near N, thereby increasing the high-frequency variability and increasing the frequency of quenching events. In all of the approaches used here, if the time series include sufficient high-frequency variability, the quenching effect reduces the ice occurrence of homogeneous

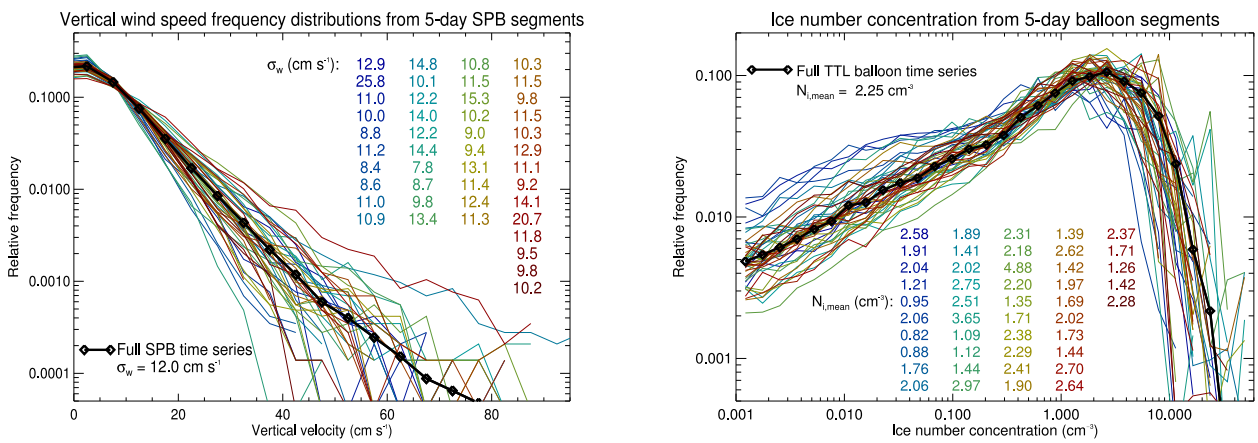

Figure 15. Vertical wind speed frequency distributions (left panel) and simulated ice concentration frequency distributions (right panel). Thick black curves: including all data from the three Stratéole-2 TTL balloons. Colored curves: results from 5-day subsets of the balloon time series.

freezing events producing high ice concentrations. However, as noted above, the mean ice concentration is not strongly affected by the quenching effect.

Above, we showed the distribution of vertical wind speed standard deviation from 5-day subsets of the Stratéole-2 data (Figure 4). Here, we use the individual 5-day time series from these segments to run ensembles if ice nucleation calculations. The vertical wind speed frequency distributions and ice concentration distributions corresponding to the 44 5-day segments are shown in Figure 15. The mean ice concentrations corresponding to the segments range from 0.8 to 4.9 cm^{-3}. In other words, the natural variability in TTL wave properties translates to considerable variability in the concentration of ice crystals produced by homogeneous freezing.

7. Summary and Discussion

In this study, we have examined the impact of variations in gravity wave-driven vertical wind speed and temperature variability on ice number concentrations produced by homogeneous freezing in the tropical tropopause layer. We quantified the variability in vertical wind speed frequency distribution using measurements from the Stratéole-2 superpressure balloon flights. We ran numerical simulations of homogeneous freezing events driven by synthetic time series of vertical wind speed generated with two different approaches, as well as directly forcing the model with time series of vertical wind from the superpressure balloon measurements. We compared the probability distributions of vertical wind speed and corresponding ice concentrations produced by homogeneous freezing from these different approaches. We further examined the sensitivities of ice number concentration statistics to wave properties such as the standard deviation of vertical wind speed and the maximum wave frequency included in the synthetic time series. In addition, we derived analytic expressions for the mean ice concentration and the probability distribution of ice concentrations produced by homogeneous freezing with wave-driven temperature variability. Key results are summarized as follows:

- High-frequency gravity waves (frequencies approaching the Brunt-Väisälä frequency) dominate the occurrence of relatively large vertical wind speeds (Figures 1 and 2).
- Using 5-day subsets of the Stratéole-2 balloon time series, we show that vertical wind speed standard deviation ranges from about 10 to 22 cm s^{-1} at different times and locations in the TTL. The corresponding range of temperature perturbation standard deviation is about 0.9K–1.6K (Figure 4).
- Eliminating high-frequency variability from the time series of vertical wind perturbations reduces the width of the vertical wind speed frequency distribution and correspondingly substantially reduces the occurrence of ice number concentrations greater than 1 cm^{-3} produced by homogeneous freezing (Figure 9).
- The analytic expressions for mean ice number concentration and ice size distribution reproduce the dependencies on maximum wave frequency and vertical wind speed standard deviation indicated by the numerical simulations (Figures 9c–11).
- Although truncating high frequencies and reducing amplitudes across all frequencies can produce nearly identical vertical wind speed frequency distributions, the resulting ice concentration frequency distributions are quite different (Figure 12). Specifically, truncating the high-frequency variability primarily eliminates the largest ice number concentrations, whereas reducing amplitudes across the board shifts the entire ice concentration frequency distribution toward smaller number concentrations.
- If the vertical wind speed standard deviation is fixed, then reducing high-frequency variability can increase the mean ice concentration by reducing the occurrence frequency of nucleation quenching events (Figures 12–14).
- The observed variability in TTL wave properties results in mean ice concentrations produced from homogeneous freezing ranging from 0.8 to 4.9 cm^{-3} (Figure 15).

The essential finding here is that observed variations in TTL gravity wave characteristics can result in substantially different ice number concentrations produced by homogeneous freezing. Further, the details of the wave spectrum (not just the frequency distribution of vertical wind speeds) are important for the resulting ice concentrations. Since wave amplitudes and power spectra change systematically with distance from deep convection, the microphysical properties of TTL cirrus likely also depend on the distance from convection.

The analytic expression for the ice number concentration frequency distribution rolls off faster at low concentrations than indicated by the numerical results (Figure 11). We hypothesize that this discrepancy is a result of the nucleation quenching effect that occurs when high-frequency variations change the temperature tendency from cooling to warming in the middle of a nucleation event, resulting in smaller ice number concentrations. This

mechanism is included in the numerical simulations but not in the analytic model. Note that when we use vertical wind speed time series without high-frequency variability, the analytic solution does a better job of reproducing the low ice concentration end of the frequency distribution.

Further analysis of nucleation events shows that reducing high-frequency variability reduces the occurrence frequency of vertical wind speed reversals during nucleation events (the quenching effect). In addition, we show that quenched homogeneous freezing events dominate for cases where the nucleated ice concentration is less than about 0.1–1 cm^{-3}, whereas unquenched nucleation events produce almost all of the higher ice concentrations. Therefore, high-frequency vertical wind speed variability can either increase or decrease ice concentrations produced by homogeneous freezing. The high-frequency waves enhance the occurrence of ice concentrations greater than about 1 cm^{-3} by increasing the occurrence frequency of strong vertical winds. However, high-frequency waves also tend to increase the occurrence of quenched nucleation events that produce lower ice concentrations. The net effect of changing high-frequency waves depends on how the overall variance of vertical wind speed changes. If the high frequency waves are added without changing the rest of the wave spectrum, then ice concentrations will increase. If the variance of vertical wind speed is fixed, then adding high-frequency waves can reduce the mean ice concentration.

The ice concentrations produced by homogeneous freezing presented here (often exceeding 1 cm^{-3}) are considerably larger than average ice concentrations measured in TTL cirrus (typically on the order of 0.1 cm^{-3}) (Jensen et al., 2018; Krämer et al., 2020; Woods et al., 2018). However, the ice concentrations shown here are the peak values just after nucleation events, whereas the measurements randomly sample all stages of the cloud lifecycles. Ice number concentrations decrease as clouds evolve due to a variety of processes, such as entrainment, dispersion, and differential sedimentation. Note that ice concentrations exceeding 1 cm^{-3} (and even exceeding 10 cm^{-3}) have been measured in TTL cirrus (Jensen et al., 2022). The high ice concentrations generally occur in small, localized patches, but these events provide the initial conditions that lead to extensive, persistent cirrus.

Conflict of Interest

The authors declare no conflicts of interest relevant to this study.

Availability Statement

The NASA airborne measurements of temperature, pressure, and vertical wind speed from the ATTREX campaign are available from (NASA/LARC/SD/ASDC, 2015). The Strateole-2 superpressure balloon measurements can be obtained from Herzog (2019).

Acknowledgments
This reasearch was supported by NSF grant number 2231667.

References

Bardeen, C. G., Toon, O. B., Jensen, E. J., Marsh, D., & Harvey, V. L. (2008). Numerical simulations of the three-dimensional distribution of meteoric dust in the mesosphere and upper stratosphere. *Journal of Geophysical Research*, *113*(D17202). https://doi.org/10.1029/2007JD009515

Boccara, G., Hertzog, A., Vincent, R. A., & Vial, F. (2008). Estimation of gravity wave momentum flux and phase speeds from quasi-Lagrangian stratospheric balloon flights. Part I: Theory and simulations. *Journal of the Atmospheric Sciences*, *65*(10), 3042–3055. https://doi.org/10.1175/2008JAS2709.1

Corcos, M., Hertzog, A., Plougonven, R., & Podglajen, A. (2021). Observation of gravity waves at the tropical tropopause using superpressure balloons. *Journal of Geophysical Research*, *126*(15), e2021JD035165. https://doi.org/10.1029/2021JD035165

Corcos, M., Hertzog, A., Plougonven, R., & Podglajen, A. (2023). A simple model to assess the impact of gravity waves on ice-crystal populations in the tropical tropopause layer. *Atmospheric Chemistry and Physics*, *23*(12), 6923–6939. https://doi.org/10.5194/acp-23-6923-2023

Dinh, T. P., Podglajen, A., Hertzog, A., Legras, B., & Plougonven, R. (2016). Effect of gravity wave temperature fluctuations on homogeneous ice nucleation in the tropical tropopause layer. *Atmospheric Chemistry and Physics*, *16*(1), 35–46. https://doi.org/10.5194/acp-16-35-2016

Forster, P. M. F., & Shine, K. P. (2002). Assessing the climate impact of trends in stratospheric water vapor. *Geophysical Research Letters*, *29*(6), 10–1/4. https://doi.org/10.1029/2001gl013909

Haladay, T., & Stephens, G. L. (2009). Characteristics of tropical thin cirrus clouds deduced from joint CloudSat and CALIPSO measurements. *Journal of Geophysical Research*, *114*(D8). https://doi.org/10.1029/2008JD010675

Hertzog, A., Cocquerez, P., Guilbon, R., Valdivia, J.-N., Venel, S., Basdevant, C., et al. (2007). Stratéole/Vorcore–Long-duration, superpressure balloons to study the Antarctic lower stratosphere during the 2005 winter. *Journal of Atmospheric and Oceanic Technology*, *24*(12), 2048–2061. https://doi.org/10.1175/2007JTECHA948.1

Herzog, A. (2019). STRATEOLE2 - C0: TSEN - Thermodynamics SENsor [Dataset]. *LMD/IPSL*. https://doi.org/10.14768/7396b9ec-582f-4be2-8c37-c34ef41247a7

Jensen, E. J., Diskin, G., DiGangi, J., Woods, S., Lawson, R. P., & Bui, T. V. (2022). Homogeneous freezing events sampled in the Tropical Tropopause Layer. *Journal of Geophysical Research*, *127*(127), e2022JD036535. https://doi.org/10.1029/2022JD036535

Jensen, E. J., Pfister, L., Jordan, D. E., Bui, T. V., Ueyama, R., Singh, H. B., et al. (2017). The NASA Airborne Tropical TRopopause EXperiment (ATTREX): High-altitude aircraft measurements in the tropical western Pacific. *Bulletin America Meteorology Social*, *1*. https://doi.org/10.1175/BAMS-D-14-00263.1

Jensen, E. J., Kärcher, B., Ueyama, R., Pfister, L., Bui, T. V., Diskin, G. S., et al. (2018). Heterogeneous ice nucleation in the tropical tropopause layer. *Journal of Geophysical Research*, *123*(21), 123. https://doi.org/10.1029/2018JD028949

Jensen, E. J., & Pfister, L. (2004). Transport and freeze-drying in the tropical tropopause layer. *Journal of Geophysical Research*, *109*(D02207). https://doi.org/10.1029/2003JD004022

Jensen, E. J., Pfister, L., Bui, T.-P., Lawson, P., & Baumgardner, D. (2010). Ice nucleation and cloud microphysical properties in tropical tropopause cirrus. *Atmospheric Chemistry and Physics*, *10*(3), 1369–1384. https://doi.org/10.5194/acp-10-1369-2010

Jensen, E. J., & Toon, O. B. (1994). Ice nucleation in the upper troposphere: Sensitivity to aerosol number density, temperature, and cooling rate. *Geophysical Research Letters*, *21*(18), 2019–2022. https://doi.org/10.1029/94gl01287

Jensen, E. J., Toon, O. B., Drdla, K., & Tabazadeh, A. (2002). Impact of polar stratospheric cloud particle composition, number density, and lifetime on denitrification. *Journal of Geophysical Research*, *107*(D20). https://doi.org/10.1029/2001JD000440

Jensen, E. J., Ueyama, R., Pfister, L., & Atlas, R. L. (2025). The impacts of gravity waves and wind shear on the lifecycle of cirrus clouds in the Tropical Tropopause Layer. *Journal of Geophysical Research*, *130*(10), e2024JD042308. https://doi.org/10.1029/2024JD042308

Jensen, E. J., Ueyama, R., Pfister, L., Bui, T. V., Alexander, M. J., Podglajen, A., et al. (2016). High-frequency gravity waves and homogeneous ice nucleation in tropical tropopause layer cirrus. *Geophysical Research Letters*, *43*(12), 6629–6635. https://doi.org/10.1002/2016gl069426

Kärcher, B., & Lohmann, U. (2002). A parameterization of cirrus cloud formation: Homogeneous freezing of supercooled aerosols. *Journal of Geophysical Research*, *107*(4010). https://doi.org/10.1029/2001JD000470

Kärcher, B., & Podglajen, A. (2019). A stochastic representation of temperature fluctuations induced by mesoscale gravity waves. *Journal of Geophysical Research*, *124*(21), 11506–11529. https://doi.org/10.1029/2019JD030680

Koop, T., Luo, B., Tsias, A., & Peter, T. (2000). Water activity as the determinant for homogeneous ice nucleation in aqueous solutions. *Nature*, *406*(6796), 611–614. https://doi.org/10.1038/35020537

Kottayil, A., A. Podglajen, A., Legras, B., Atlas, R., Prajwal, K., Satheesan, K., & Abhilash, S. (2024). High-frequency gravity waves and Kelvin-Helmholtz billows in the tropical UTLS, as seen from radar observations of vertical wind. *Geophysical Research Letters*, *51*(21), e2024GL110366. https://doi.org/10.1029/2024GL110366

Krämer, M., Rolf, C., Spelten, N., Afchine, A., Fahey, D., Jensen, E., et al. (2020). A microphysics guide to cirrus—Part II: Climatologies of clouds and humidity from observations. *Atmospheric Chemistry and Physics*, *20*, 20. https://doi.org/10.5194/acp-20-12569-2020

Massman, W. J. (1978). On the nature of vertical oscillations of constant volume balloons. *Journal of Applied Meteorology*, *17*(9), 1351–1356. https://doi.org/10.1175/1520-0450(1978)017<1351:otnovo>2.0.co;2

NASA/LARC/SD/ASDC. (2015). *Attrex global hawk UAS meteorological and navigational measurements*. NASA Langley Atmospheric Science Data Center DAAC. https://doi.org/10.5067/AIRCRAFT/ATTREX/CLOUD-H2O-TRACER-RADIATION

Nastrom, G. D. (1980). The response of superpressure balloons to gravity waves. *Journal of Applied Meteorology*, *19*(8), 1013–1019. https://doi.org/10.1175/1520-0450(1980)019⟨1013:trosbt⟩2.0.co;2

Podglajen, A., Hertzog, A., Plougonven, R., & Legras, B. (2016). Lagrangian temperature and vertical velocity fluctuations due to gravity waves in the lower stratosphere. *Geophysical Research Letters*, *43*(7), 3543–3553. https://doi.org/10.1002/2016GL068148

Podglajen, A., Hertzog, A., Plougonven, R., & Žagar, N. (2016). Assessment of the accuracy of (re)analyses in the equatorial lower stratosphere. *Journal of Geophysical Research*, *119*(19). https://doi.org/10.1002/2014JD021849

Schneider, J., Höhler, K., Wagner, R., Saathoff, H., Schnaiter, M., Schorr, T., et al. (2021). High homogeneous freezing onsets of sulfuric acid aerosol at cirrus temperatures. *Atmospheric Chemistry and Physics*, *21*(18), 14403–14425. https://doi.org/10.5194/acp-21-14403-2021

Schoeberl, M. R., Jensen, E. J., Podglajen, A., Coy, L., Lodha, C., Candido, S., & Carver, R. (2017). Gravity wave spectra in the lower stratosphere diagnosed from Project Loon balloon trajectories. *Journal of Geophysical Research*, *122*(16), 8517–8524. https://doi.org/10.1002/2017JD026471

Scott, S. G., Bui, T. P., Chan, K. R., & Bowen, S. W. (1990). The meteorological measurement system on the NASA ER-2 aircraft. *Journal of Atmospheric and Oceanic Technology*, *7*(4), 525–540. https://doi.org/10.1175/1520-0426(1990)007<0525:tmmsot>2.0.co;2

Spichtinger, P., & Krämer, M. (2013). Tropical tropopause ice clouds: A dynamic approach to the mystery of low crystal numbers. *Atmospheric Chemistry and Physics*, *13*(19), 9801–9818. https://doi.org/10.5194/acp-13-9801-2013

Toon, O. B., Turco, R. P., Westphal, D., Malone, R., & Liu, M. S. (1988). A multidimensional model for aerosols: Description of computational analogs. *Journal of the Atmospheric Sciences*, *45*(15), 2123–2143. https://doi.org/10.1175/1520-0469(1988)045<2123:ammfad>2.0.co;2

Ueyama, R., Jensen, E. J., & Pfister, L. (2018). Convective influence on the humidity and clouds in the tropical tropopause layer during boreal summer. *Journal of Geophysical Research*, *123*(14), 7576–7593. https://doi.org/10.1029/2018JD028674

Ueyama, R., Jensen, E. J., Pfister, L., & Kim, J.-E. (2015). Dynamical, convective, and microphysical control on wintertime distributions of water vapor and clouds in the tropical tropopause layer. *Journal of Geophysical Research*, *120*(19). https://doi.org/10.1002/2015JD023318

Vincent, R. A., & Hertzog, A. (2014). The response of superpressure balloons to gravity wave motions. *Atmospheric Measurement Techniques*, *7*(4), 1043–1055. https://doi.org/10.5194/amt-7-1043-2014

Wilson, R., Pitois, C., Podglajen, A., Hertzog, A., Corcos, M., & Plougonven, R. (2023). Detection of turbulence occurrences from temperature, pressure, and position measurements under superpressure balloons. *Atmospheric Measurement Techniques*, *16*(2), 311–330. https://doi.org/10.5194/amt-16-311-2023

Woods, S. R. P., Lawson, R. P., Jensen, E. J., Bui, P., Thornberry, T., Rollins, A., et al. (2018). Microphysical properties of tropical tropopause layer (TTL) cirrus. *Journal of Geophysical Research*, *123*(11), 6053–6069. https://doi.org/10.1029/2017JD028068